Optical sectioning in induced coherence tomography with frequency-entangled photons

Adam Vallés,[1,*] Gerard Jiménez,[1] Luis José Salazar-Serrano,[1] and Juan P. Torres[1,2,†]

[1]*ICFO-Institut de Ciencies Fotoniques, Barcelona Institute of Science and Technology, Mediterranean Technology Park, 08860 Castelldefels, Barcelona, Spain*

[2]*Department of Signal Theory and Communications, Universitat Politecnica de Catalunya, Campus Nord D3, 08034 Barcelona, Spain*

We demonstrate a different scheme to perform optical sectioning of a sample based on the concept of induced coherence [Zou *et al.*, Phys. Rev. Lett. **67**, 318 (1991)]. This can be viewed as a different type of optical coherence tomography scheme where the varying reflectivity of the sample along the direction of propagation of an optical beam translates into changes of the degree of first-order coherence between two beams. As a practical advantage the scheme allows probing the sample with one wavelength and measuring photons with another wavelength. In a bio-imaging scenario, this would result in a deeper penetration into the sample because of probing with longer wavelengths, while still using the optimum wavelength for detection. The scheme proposed here could achieve submicron axial resolution by making use of nonlinear parametric sources with broad spectral bandwidth emission.

I. INTRODUCTION

In 1991, Huang *et al.* [1] put forward a three-dimensional noninvasive optical imaging technique that permits cross-sectional and axial high-resolution tomographic imaging of biological tissue. They named the new technique optical coherence tomography (OCT) and demonstrated it obtaining high-resolution images of the layers that make up the retina. The axial and transverse resolutions of OCT are independent. To obtain information in the transverse direction (plane perpendicular to the beam propagation), OCT focuses light to a small spot that is scanned over the sample. To obtain information in the axial direction (along the beam propagation), OCT uses a source of light with short coherence length that allows optical sectioning of the sample.

In the same year, Zou *et al.* [2] introduced the concept of *induced coherence*. When two second-order nonlinear crystals (NLC$_1$ and NLC$_2$) are optically pumped by a coherent wave, a pair of signal and idler photons might emerge (signal s_1 and idler i_1 from NLC$_1$; signal s_2 and idler i_2 from NLC$_2$) by means of the nonlinear process of parametric down-conversion. Most experiments are usually done in the regime of very low parametric gain (weak pumping) so that paired photons are expected to be generated in one or the other crystal [3].

In the absence of any other injected signal or idler beams, the two signal beams show no first-order coherence ($|g^{(1)}_{s_1,s_2}| = 0$) [4,5] and thus do not give rise to interference when recombined in a beam splitter [6]. However, if idler i_1 is injected into the second nonlinear crystal and the experimental configuration is designed to make idlers i_1 and i_2 indistinguishable after NLC$_2$, the signal photons s_1 and s_2 will show first-order coherence,

i.e., $|g^{(1)}_{s_1,s_2}| = 1$. If idler i_1 traverses an element with reflectivity τ before impinging on NLC$_2$ (or transmissivity μ depending on the setup configuration), there is a loss of first-order coherence between the signal photons coming out from the two nonlinear crystals. This effect could be observed in the temporal [2] and frequency domains [7], and it should still be present in the case of strong pumping [8,9].

There has been a growing interest in recent years in these so-called *nonlinear interferometers* [10], not only because of their importance to unveil the interplay between information and coherence in quantum theory [11,12], but also because of their applications in quantum information and quantum metrology. For instance, Kalashnikov *et al.* [13] showed that a nonlinear interferometer allows performing spectral measurements in the infrared range using visible-spectral-range components, avoiding the use of optical equipment suited for operation in the infrared range that may have inferior performance and higher cost.

Recently Barreto *et al.* [14,15] used the concept of induced coherence to demonstrate a two-dimensional quantum imaging system, where photons used to illuminate the object do not have to be detected at all, which enables the probe wavelength to be chosen in a range for which suitable detectors are not available. We might call the imaging system *induced coherence tomography*.

Here we go one step further and demonstrate in a *proof-of-concept* experiment that a nonlinear interferometer based on the concept of induced coherence can be used to perform three-dimensional imaging of a sample, i.e., in addition to obtaining information in the transverse plane (plane perpendicular to the beam propagation), which was demonstrated in Ref. [14], it can also provide optical sectioning of the sample (information in the axial direction, along the beam propagation), which we demonstrate here.

In doing this, we put forward indeed a new type of OCT scheme based, however, on a different physical principle. This is explained with the help of Figs. 1 and 2. In OCT, different

---

*adam.valles@icfo.eu; Present address: School of Physics, University of the Witwatersrand, Private Bag 3, Johannesburg 2050, South Africa.
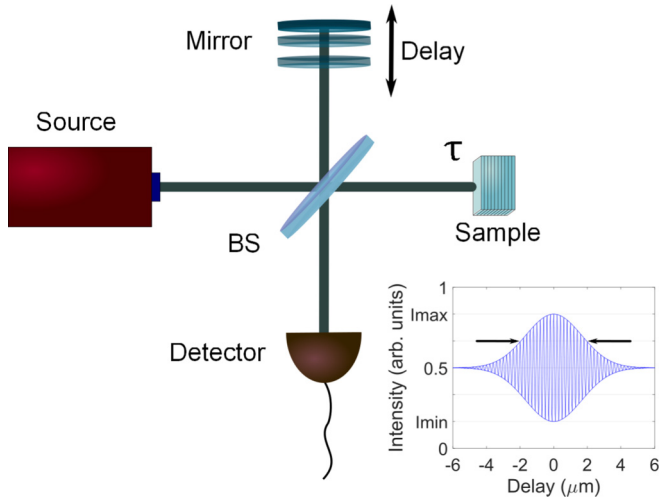
†juanp.torres@icfo.eu

FIG. 1. Sketch of a time-domain OCT scheme and typical interferogram obtained for a certain axial measurement. The interferogram shows the effect on axial resolution of the low-coherence length of the source of light.
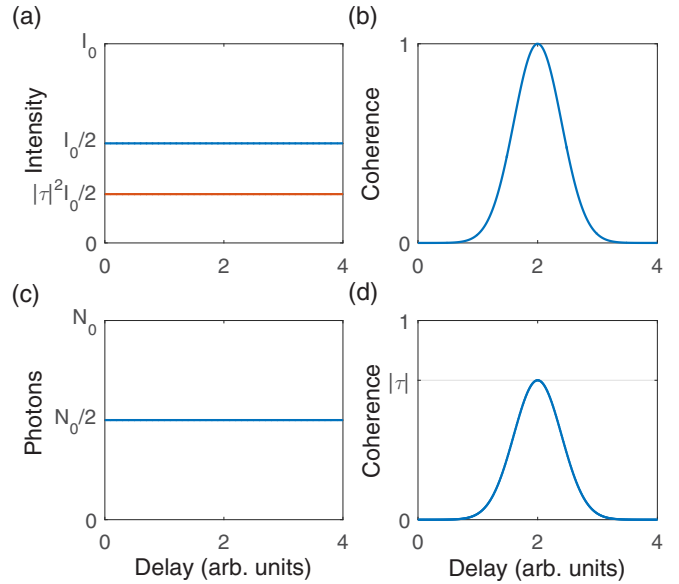

FIG. 2. Differences between a simplified but *typical* OCT scheme and the new configuration are demonstrated. (a, c) Intensity (or photon flux) traversing the reference and sample arms of the interferometer. (a) In OCT, the intensity of the reference beam is $I_0/2$, and the intensity coming from the sample is $|\tau|^2 I_0/2$. I_0 is the total intensity. (c) In our optical sectioning scheme, in the very low parametric gain regime, the two signal beams traversing each arm of the interferometer contain $N_0/2$ photons, independently of the reflectivity τ. N_0 is the total number of photons propagating through the interferometer. (b, d) Degree of first-order coherence between light beams propagating in the two arms of the interferometer. (b) Coherence in OCT, and (d) coherence in our scheme.

layers of the sample show different reflectivity (τ) or backscattering. For each axial measurement, the wave reflected from the sample and the reference wave carry different intensities, $|\tau|^2 I_0/2$ and $I_0/2$, respectively [see Fig. 2(a)]. They show first-order coherence only for a given delay [see Fig. 2(b)] and interfere for this delay with a visibility that depends on τ. OCT performs thus direct measurements of the reflectivity; it *does not measure first-order coherence* as the name of the technique might wrongly lead one to think. The low-coherence length of the source provides positioning of the reflectivity measurement, the exact depth into the sample that is being analyzed.

On the other hand, in the scheme based on induced coherence in the very low parametric gain regime, the flux of photons in the two arms of the interferometer is the same ($N_0/2$) [see Fig. 2(c)]. However, there is a loss of coherence between both beams [see Fig. 2(d)] that is due to the reflectivity of the sample (see the Appendix). Therefore, and contrary to common OCT configurations, first-order coherence plays a double role in induced coherence tomography: (1) it carries the sought-after information about the reflectivity of the sample and (2) it provides axial optical sectioning of the sample.

An OCT scheme with the word *quantum* attached to it was demonstrated some years ago [16,17]. It showed, as a characteristic element, certain immunity to the presence of depth-dependent dispersion in the sample that deteriorates the resolution achievable in an OCT scheme [18]. This dispersion cancellation effect also appears when using phase-sensitive cross-correlated beams that, however, show no entanglement [19,20]. This so-called quantum OCT scheme is fundamentally different from ours in two important aspects: first, they use entangled photons that, however, are not embedded in a nonlinear interferometer. Second, their OCT scheme is based on the measurement of second-order coherence functions (coincidence counts measurements), while our scheme makes use of first-order coherence functions, as is the case of common OCT schemes.

II. BRIEF DESCRIPTION OF THE CONCEPT OF INDUCED COHERENCE

Since the concept of induced coherence is the physical basis that makes possible the results presented in this paper, for the sake of clarity we briefly describe here the concept (see Fig. 3). For simplicity, we consider the single-mode case in this section. A more detailed description of the multimode (multifrequency) case is considered in the Appendix.

Two second-order nonlinear crystals are coherently pumped by a strong pump beam. In the first nonlinear crystal (NLC$_1$), pairs of signal (annihilation operator a_{s_1}) and idler (a_{i_1}) photons are generated by means of the spontaneous parametric down-conversion process (SPDC). The relationship between the input (b_s and b_i) and output operators (a_{s_1} and a_{i_1}) can be described by a Bogoliubov transformation [21–23]:

$$a_{s_1} = U b_s + V b_i^\dagger,$$
$$a_{i_1} = U b_i + V b_s^\dagger, \tag{1}$$

where $|U|^2 - |V|^2 = 1$. The idler photon traverses a lossy object with transmissivity μ:

$$a_{i_1} \Longrightarrow \mu a_{i_1} + f, \tag{2}$$

being $[f, f^\dagger] = 1 - |\mu|^2$ [24,25].

After traversing the lossy object, i_1 enters the second nonlinear crystal (NLC$_2$). The annihilation operator of signal
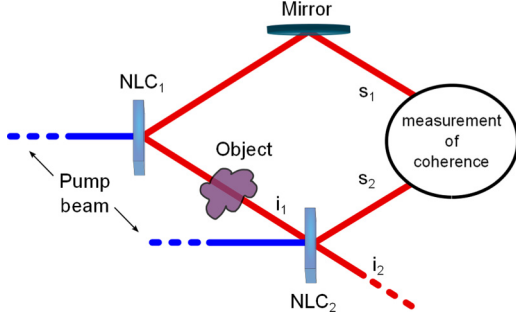
FIG. 3. Simplified sketch of a nonlinear interferometer aimed at introducing the concept of induced coherence by using two nonlinear crystals (NLC$_{1\&2}$).

s_2 after the second nonlinear crystal is

$$a_{s_2} = U c_s + V[\mu^* a_i^\dagger + f^\dagger]$$
$$\implies a_{s_2} = U c_s + |V|^2 \mu^* b_s + V U^* \mu^* b_i^\dagger + V f^\dagger, \quad (3)$$

where c_s is the input signal operator in the second nonlinear crystal.

The degree of coherence between the two signal waves, s_1 and s_2, can be quantified by the normalized degree of first-order coherence, which reads

$$g_{s_1,s_2}^{(1)} = \frac{\langle a_{s_1}^\dagger a_{s_2} \rangle}{\sqrt{\langle a_{s_1}^\dagger a_{s_1} \rangle} \sqrt{\langle a_{s_2}^\dagger a_{s_2} \rangle}}. \quad (4)$$

If the quantum states corresponding to the operators b_s, b_i, and c_s are the vacuum state, the flux rate of s_1 photons is $\langle a_{s_1}^\dagger a_{s_1} \rangle = |V|^2$, and the flux rate of s_2 photons is $\langle a_{s_2}^\dagger a_{s_2} \rangle = |V|^2[1 + |\mu|^2 |V|^2]$. We can obtain [8,9]

$$\left| g_{s_1,s_2}^{(1)} \right| = |\mu| \sqrt{\frac{1 + |V|^2}{1 + |\mu|^2 |V|^2}}. \quad (5)$$

If $|\mu| = 1$ there is first-order coherence between the two signals. Injection of i_1 into the second nonlinear induces coherence between signals s_1 and s_2. Notice that it is important that idler i_2 is indistinguishable from idler i_1 after the second nonlinear crystal. This is why sometimes the induced coherence is related to the indistinguishability of the idler waves.

If $|\mu| = 0$, there is no first-order coherence between signals, since

$$a_{s_1} = U b_s + V b_i^\dagger,$$
$$a_{s_2} = U c_s + V f^\dagger, \quad (6)$$

and $\langle b_s^\dagger c_s \rangle = 0$ and $\langle b_i f^\dagger \rangle = 0$. In this case, we have two independent spontaneous parametric down-conversion processes; therefore the resulting signal waves show no coherence. In an intermediate case, there is partial coherence between the two signal waves.

Under most circumstances, as is the case here, experiments work in the low parametric gain regime, where V is extremely

small ($|V| \ll 1$), so $|U| \sim 1$. In this case, we have

$$\left| g_{s_1,s_2}^{(1)} \right| = |\mu|. \quad (7)$$

In this scenario a pair of signal-idler photons is generated in one crystal or the other, since the probability to generate two pairs of signal-idler photons is extremely low.

III. EXPERIMENTAL SETUP

Figure 4 depicts the experimental setup. The laser that pumps the two nonlinear crystals is a high-power continuous-wave (CW) Verdi V10 (Coherent, wavelength of 532 nm). The path difference traveled by the pump beam in its way towards the two nonlinear crystals should be smaller than the coherence length of the pump beam to allow interference between the down-converted photons [26]. The pump beam is split with a 50:50 beam splitter (BS), so that the same pump power impinges on two periodically polled lithium niobate crystals (PPLN$_1$ and PPLN$_2$). These crystals mediate the absorption of a 532 nm pump photon and the generation of two lower-frequency photons, signal and idler, by means of SPDC. The process is nondegenerate type-0, meaning that all three photons, pump, signal, and idler, have the same vertical polarization. Signal and idler photons are generated with different central wavelengths, 810 nm and 1550 nm, respectively. The efficiency of the SPDC process is extremely low, so we can neglect the probability to generate two pairs of signal-idler photons, each pair in a different crystal, at the same time.

Signal and idler photons leaving PPLN$_1$ are separated by a dichroic mirror (DM$_1$). The 810 nm signal photon is transmitted, forming the upper arm of the Mach-Zehnder interferometer. Its polarization is changed with the help of the half-wave plate (HWP$_2$) and joins the signal photon coming from PPLN$_2$ at the polarization beam splitter (PBS$_2$). Both signal photons have orthogonal polarizations before reaching PBS$_2$. The measurement is carried out by detecting the polarization state of the 810 nm signal photons after PBS$_2$. If there is coherence between signal photons ($|\tau| = 1$) the polarization state after PBS$_2$ will be

$$|\Psi\rangle = \frac{1}{\sqrt{2}} \{|H\rangle + \exp(i\phi)|V\rangle\}, \quad (8)$$

where ϕ is the phase difference between the two interfering arms, introduced by the temporal delay stage. Whereas if there is no polarization coherence ($|\tau| = 0$), the polarization state will read

$$\rho = \tfrac{1}{2} \{|H\rangle\langle H| + |V\rangle\langle V|\}; \quad (9)$$

therefore there will not be any phase difference dependence.

The 1550 nm idler photon coming from PPLN$_1$ is the one that interacts with the sample. It is reflected in the dichroic mirror DM$_1$, starting the lower arm of the interferometer. It is reflected again in the polarization beam splitter (PBS$_1$), due to its vertical linear polarization. It traverses a quarter-wave plate (QWP) that changes its polarization to circular. It interacts with the sample, formed by a tunable neutral density filter and a movable mirror that can be displaced longitudinally up to by 1 mm. This is equivalent to the presence of a layer of that thickness for low reflectivity values. The mirror reflects back the idler photon with probability $|\tau|^2$. The QWP changes its polarization to horizontal. This photon, now carrying the

FIG. 4. Experimental setup for observing optical sectioning based on the concept of induced coherence. Laser: Verdi V10; Optical system: linear attenuator and short-pass filter; BS: beam splitter for the pump beam; $PPLN_{1\&2}$: periodically polled lithium niobate (nonlinear crystals); $DM_{1\&2}$: dichroic mirrors; Sample: mirror and a variable neutral density filter; Temporal delay: 6-mm-long stepper motor; QWP: quarter-wave plate; $HWP_{1\&2}$: half-wave plates; D_1: optical spectrum analyzer (OSA) at the telecom wavelength; D_2: single-photon counting module; M: mirrors; P: polarizer; BPF: band-pass filter; H and V: horizontal and vertical polarizations, respectively, and the subindex indicates the wavelength of the beam. For the sake of simplicity, focal distances and position of lenses are not shown. However, the exact position of the lenses in the lower interference arm before the $PPLN_2$ has an important role when the distinguishability between the two idler spatial modes is at stake.

information of the sample (τ), is transmitted through PBS_1 due to its horizontal polarization. Later it is rotated again to vertical polarization with a half-wave plate (HWP_1) in order to erase all distinguishing information with respect to the second 1550 nm idler photon. With another dichroic mirror DM_1, the 1550 nm idler photon that is generated in the first nonlinear crystal and probed the sample overlaps spatially with the pump beam that illuminates the second nonlinear crystal, and consequently also with the second 1550 nm idler photon.

After the second nonlinear crystal ($PPLN_2$), the second signal photon is separated from the two spatially overlapping idler photons, which are reflected in DM_1 and coupled into a single-mode fiber for alignment purposes. The second 810 nm signal photon continues the lower interferometer arm until it reaches PBS_2. A temporal delay is implemented in the upper arm of the interferometer, formed by two mirrors on top of a platform that can move in steps of the order of tens of nanometers because of a 6-mm stepper motor (Thorlabs Z806) attached to it.

The two 20-mm-long PPLN crystals are mounted on top of ovens (Covesion), being able to adjust their temperature by a tenth of degree Celsius. This change of temperature induces a variation in the spectral response of the nonlinear crystals, leading to different phase-matching conditions for each temperature. In order to oversee the spectral overlap between idler photons originated in the two PPLN crystals, its spectrum is measured with an optical spectrum analyzer (OSA). Notwithstanding, the detection of the 1550 nm photons is not necessary for the correct functioning of the OCT scheme; its detection serves only for monitoring and alignment purposes.

The pump beam at 532 nm is separated from the signal after being reflected in the dichroic mirror DM_2. The residual

pump power still existing at the output of PBS_2, overlapping with the two orthogonally polarized 810 nm signal photons, is filtered out by a band-pass filter (BPF). We also implement a polarizer (P) that projects the incoming signal photons into the polarization diagonal state,

$$|D\rangle = \frac{1}{\sqrt{2}}\{|H\rangle + |V\rangle\}, \tag{10}$$

being able to measure the phase dependence given in Eq. (8). Finally, the interference signal is coupled into a single-mode fiber and measured with a silicon-based single photon detector (Perkin-Elmer).

The results presented in the next section are interferometric measurements, and for the sake of clarity, we summarize here what constitutes the interferometer. The Mach-Zehnder interferometer starts in $PPLN_1$. The upper arm is formed by the 810 nm signal photon generated in the first nonlinear crystal until it reaches the polarization beam splitter PBS_2. The lower arm is formed by the 1550 nm idler photon generated also in the first nonlinear crystal, until it reaches the second nonlinear crystal ($PPLN_2$). It continues with the 810 nm signal photon generated in the second nonlinear crystal until it reaches the other input port of the polarization beam splitter PBS_2.

IV. RESULTS

Figure 5 shows the measurement of the degree of first-order coherence between signal photons, when the idler photon generated in the first nonlinear crystal is reflected from a mirror ($|\tau| = 1$) that can be moved between two positions. Note that this is a *proof-of-concept* experiment, and the axial resolution
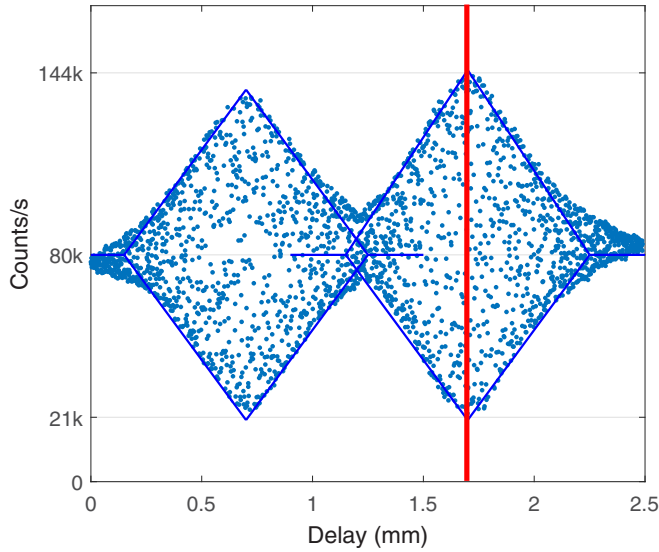
FIG. 5. Degree of first-order coherence measured from two layers separated 1 mm apart. We detect 809.4 nm photons with diagonal polarization at the output of PBS$_2$, changing the path difference between the two arms of the interferometer in micrometric steps (1 μm) for every point depicted. We obtain a maximum interference visibility of $V = 73\%$, within the region marked in red. Blue dots correspond to experimental data, and the solid curve stands for the theoretical prediction given by Eq. (11), taking into account our given visibility values.

obtained (500 μm) can be readily improved, as will be shown below in the discussion section. The key element that makes our optical sectioning scheme work is that the visibility of the interference of signal photons can be controlled by insertion of different temporal delays between the idler photons [27]. The curve measured, for any of the two peaks, shows clearly a correlation function with a triangular shape

$$\left|g_{s_1,s_2}^{(1)}(T)\right| = \frac{|\langle a_{s_1}^\dagger(t+T)a_{s_2}(t)\rangle|}{\sqrt{\langle a_{s_1}^\dagger(t)a_{s_1}(t)\rangle}\sqrt{\langle a_{s_2}^\dagger(t)a_{s_2}(t)\rangle}}$$
$$= \mathrm{tri}\left\{\frac{1}{DL}[T-T_0]\right\}, \quad (11)$$

where "tri" is the triangular function (see the Appendix), D is the difference of inverse group velocities between signal and idler photons, L is the nonlinear crystal length, and T_0 (cT_0 spatial delay) is the temporal delay between signal photons, necessary to obtain maximum coherence between them (see the Appendix). The temporal resolution is given by DL, which is the inverse bandwidth of the source of photons and proportional to the coherence length. The spatial resolution in free space is thus cDL, the axial resolution of our optical sectioning scheme.

The visibility of the left peak of the correlation function shown in Fig. 5 is different than the one of the right peak, with a value of $V = 73\%$. The difference is caused by the fact that signal coupling optimization was performed for one location of the mirror, so when displaced, a small decrease of visibility can be expected. In these results we made use of the full bandwidth of the paired photons generated in both crystals,
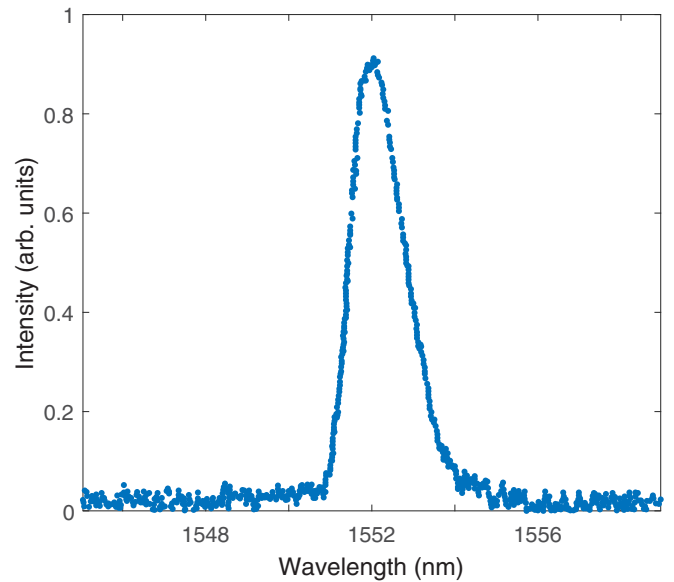
FIG. 6. Measured spectrum of the idler photons. The spectrum is centered at 1552.3 nm with a bandwidth of 1.6 nm at full-width at half maximum (FWHM).

changing the difference between path length of the two arms of the interferometer in micrometric steps (1 μm).

The coherence length and shape of the coherence functions are directly related with the shape and bandwidth of the emitting source, shown in Fig. 6. In our case, the 20-mm-long PPLN type-0 crystal generates an idler spectral emission bandwidth of about 1.6 nm at full-width at half maximum (FWHM), measured with an OSA. Measurements showed that the spectrum of photon pairs generated in each crystal is slightly different. This is a source of spectral distinguishability between photons coming from different crystals, and therefore of loss of coherence and decrease of visibility.

In order to demonstrate that we are observing induced coherence in the low parametric gain regime, we should obtain experimentally the expected relationship between visibility and reflectivity, i.e., $V = |\tau|$ (see Ref. [2] and the Appendix). Figures 7 and 8, apart from showing such relationship, also aim at demonstrating that one can obtain the high visibility, $V = 90\%$ in our case, necessary to reach high sensitivity when mapping layer reflectivities. The erasure of distinguishability between paired photons generated in different nonlinear crystals is in general a highly demanding experimental task. In a recent work, Barreto *et al.* [14] obtained a maximum visibility of $V = 77\%$. In the original paper from 1991 where the idea of induced coherence was introduced by Zou *et al.* [2], they were able to obtain a visibility of $V = 30\%$. These values from previous experiments show how difficult it can be to successfully overlap spatial modes when large bandwidths are considered, and to compensate all the different degrees of freedom involved in the system that can provide unwanted path distinguishability.

Figure 7 shows the number of signal photons detected at the output of PBS$_2$ with respect to variations in length of both arms of the interferometer. Interference fringes appear for $|\tau| = 1$. We marked with a red rectangle in Fig. 5 the small
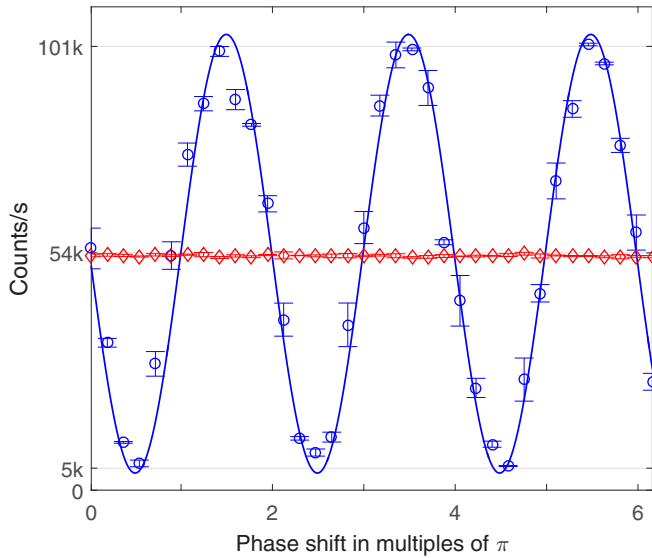
FIG. 7. Interference fringes for different values of the reflection coefficient (τ) measured with nanometric steps within the red area marked in Fig. 5. Circles: $|\tau| = 1$; diamonds: $|\tau| = 0$. The maximum visibility measured is $V = 90\%$. The error bars designate the standard deviation of the experimental measures.
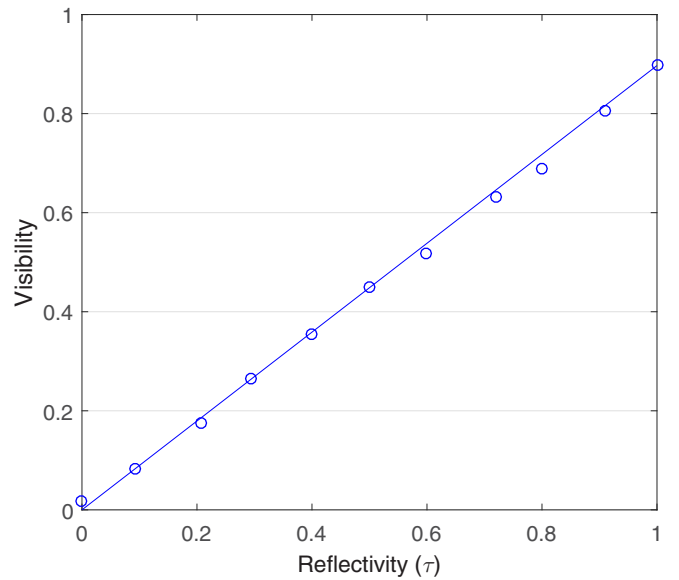

FIG. 8. Experimental relation between the visibility of the interference pattern and the reflectivity of the simulated sample. Open circles correspond to experimental measurements, and the solid curve stands for the theoretical prediction for our particular visibility conditions, taking into account the characterized transmission values of our neutral density filter.

area that corresponds to the results shown in Fig. 7. We show (red diamonds) the effect of blocking the first 1550 nm idler photon.

In these measurements the bandwidth of the signal photons is filtered with the help of a 8-mm fiber Bragg grating (FBG). The central wavelength of the FBG filters at room temperature is at 809.4 nm. This central wavelength can be modified by changing the temperature of the FBG or stretching it, but we decided to change the temperatures of the PPLN ovens instead. For that reason the central wavelength of the SPDC idler spectrum in Fig. 6 is around 1552.3 nm.

The purpose of filtering the signal photons with the FBG is twofold. On the one hand, filtering out the bandwidth helps to reduce the distinguishability of paired photons that originates in different nonlinear crystals, erasing the undesired spectral distinguishability. For that reason, the maximum visibility measured in Fig. 7 increases up to $V = 90\%$. On the other hand, the coherence length turns out to be of the order of tens of centimeters. This is due to the narrow bandwidth ($B_s \sim 0.1$ nm) that is reflected from the FBG. Therefore axial resolution degrades. Figure 8 depicts the experimental relationship between the visibility of the interference pattern and the reflectivity of the sample. We note that all results shown in this paper are raw experimental data with the dark counts subtraction ($\sim$2k) from the single-photon counting modules.

V. DISCUSSION AND CONCLUSIONS

As a general rule in OCT, the broader the bandwidth of the spectrum, the better the axial resolution. For the sake of comparison, *typical* OCT configurations available commercially make use of broadband light sources, with a spectral emission of more than 100 nm at full-width at half maximum. In this way they are able to perform measurements with axial resolutions of the order of few microns, as shown in the inset

of Fig. 1. One can achieve resolutions of a few nanometers (as narrow as 8 nm) [28,29] by using extreme ultraviolet radiation. This would allow material identification and opaque matter penetration, but would be harmful for biological tissues.

We can increase the resolution of the optical sectioning scheme put forward here by increasing the bandwidth of down-converted photons. Broader bandwidths can be obtained by using shorter crystals or by appropriately engineering the phase-matching conditions of longer crystals [30,31]. In this way, axial resolutions similar to the ones achieved with current OCT systems are likely to be observed.

In conclusion, we have introduced the basic principles of an optical sectioning imaging system that can be called *induced coherence tomography*, a type of OCT scheme based on the concept of induced coherence. We have demonstrated it using frequency-entangled photons generated in SPDC processes embedded in a nonlinear interferometer. Notwithstanding, Shapiro *et al.* [32] have shown that similar results can also be obtained using a pair of bright pseudothermal beams possessing a phase-sensitive cross correlation.

From a fundamental point of view, our scheme is a coherence measurement, in contrast to *conventional* OCT schemes that measure directly reflectivity. In our scheme, the change of reflectivity induces a change of first-order coherence between two streams of photons that are made to interfere. From a practical point of view, the photons that are being measured never interact with the sample. That is to say, we are able to detect photons centered at a wavelength with the maximum efficiency of silicon-based detectors, while the sample is being probed with photons centered at NIR. This could potentially be used in biological tissue to image even deeper into the tissue with the use of longer wavelengths.

APPENDIX

First-order coherence is the main tool in our *induced coherence tomography* scheme. In this appendix we calculate the value of the normalized first-order correlation function between signal photons that are generated in different nonlinear crystals, depicted in Fig. 5.

A CW plane-wave pump beam with frequency ω_p and flux of pump photons of F_0 photons/s/m^2 illuminates a second-order nonlinear crystal of length L and nonlinear coefficient $\chi^{(2)}$. The molecules or atoms of the crystal mediate the generation of paired photons (signal and idler) by means of the nonlinear process of spontaneous parametric down-conversion (SPDC).

The electric field operators of signal and idler photons read

$$E_s^+(t,z) = \frac{1}{(2\pi)^{1/2}} \int d\Omega \left[\frac{\hbar\omega_s}{2\epsilon_0 c n_s}\right]^{1/2} a_s(z,\Omega)$$
$$\times \exp\left[ik_s(\omega_s+\Omega)z - i(\omega_s+\Omega)t\right],$$

$$E_i^+(t,z) = \frac{1}{(2\pi)^{1/2}} \int d\Omega \left[\frac{\hbar\omega_i}{2\epsilon_0 c n_i}\right]^{1/2} a_i(z,\Omega)$$
$$\times \exp\left[ik_i(\omega_i+\Omega)z - i(\omega_i+\Omega)t\right]. \quad (A1)$$

We neglect all spatial dependence of the fields for the sake of simplicity.

Figure 9 shows schematically the operators at different positions inside the experimental setup, as well as the main distances between elements considered. Let $\hat{b}_s(\Omega) \equiv a_s(z=0,\Omega)$ and $\hat{b}_i(\Omega) \equiv a_i(z=0,\Omega)$ designate the operators corresponding to the signal (frequency $\omega_s+\Omega$) and idler (frequency $\omega_i-\Omega$) modes at the input face of the nonlinear crystal.
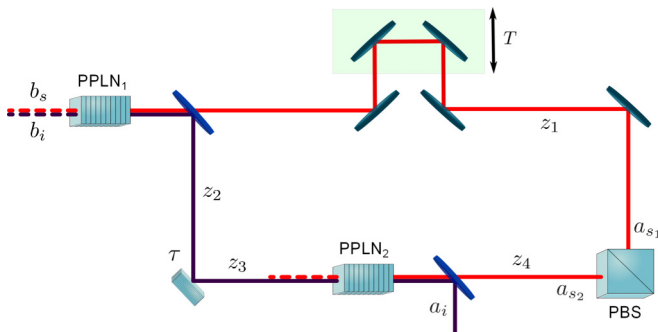

FIG. 9. Simple sketch of the experimental setup that shows the name of the operators at different locations and main distances considered in the calculation.

$a_s(\Omega) \equiv a_s(z=L,\Omega)$ and $a_i(\Omega) \equiv a_i(z=L,\Omega)$ designate the operators corresponding to the same modes at the output face of the nonlinear crystal. Under the condition that the pump beam is undepleted, since the efficiency of the parametric process is low, the relationship between input and output modes is a Bogoliubov transformation that reads as [21–23]

$$a_s(\Omega) = U(\Omega)b_s(\Omega) + V(\Omega)b_i^\dagger(-\Omega),$$
$$a_i(\Omega) = U(\Omega)b_i(\Omega) + V(\Omega)b_s^\dagger(-\Omega), \quad (A2)$$

where

$$U(\Omega) = \exp\left[i\frac{\Delta(\Omega)L}{2}\right]$$
$$\times \left\{\cosh[\Gamma(\Omega)L] - i\frac{\Delta(\Omega)}{2\Gamma(\Omega)}\sinh[\Gamma(\Omega)L]\right\},$$

$$V(\Omega) = i\frac{\sigma}{\Gamma(\Omega)}\exp\left[i\frac{\Delta(\Omega)L}{2}\right]\sinh[\Gamma(\Omega)], \quad (A3)$$

σ is the nonlinear coefficient (in units of m^{-1})

$$\sigma = \left[\frac{\hbar\omega_s\omega_i\omega_p[\chi^{(2)}]^2 F_0}{8\epsilon_0 c^2 n_s n_i n_p}\right]^{1/2}, \quad (A4)$$

the phase-matching function is

$$\Delta(\Omega) = k_p(\omega_p) - k_s(\omega_s+\Omega_s) - k_i(\omega_i-\Omega), \quad (A5)$$

and Γ reads

$$\Gamma(\Omega) = \left[\sigma^2 - \frac{\Delta^2(\Omega)}{4}\right]^{1/2}. \quad (A6)$$

The nonlinear coefficient σ is very small; therefore we can safely write $\Gamma(\Omega) \sim i\Delta(\Omega)/2$. Moreover, we expand the longitudinal wave numbers in a Taylor series, i.e., $k_j(\Omega) = k_j^0 + N_j\Omega$ ($j = s,i$). $N_{s,i}$ are inverse group velocities for the signal and idler photons. The phase-matching function now reads $\Delta(\Omega) = D\Omega$ where $D = N_i - N_s$. Under these conditions, we obtain that

$$U(\Omega) = 1,$$
$$V(\Omega) = \sigma L \, \text{sinc}\left(\frac{DL\Omega}{2}\right)\exp\left[i\frac{\Delta(\Omega)L}{2}\right]. \quad (A7)$$

The normalized first-order correlation function ($g_{s_1,s_2}^{(1)}(T)$) between signal photons generated in the first nonlinear crystal (a_{s1}) and signal photons generated in the second nonlinear crystal (a_{s2}) (what we sometimes refer to as *coherence* in the main text) writes

$$g_{s_1,s_2}^{(1)}(T) = \frac{\langle E_{s_1}^-(t+T)E_{s_2}^+(t)\rangle}{\sqrt{\langle E_{s_1}^-(t)E_{s_1}^+(t)\rangle}\sqrt{\langle E_{s_2}^-(t)E_{s_2}^+(t)\rangle}}, \quad (A8)$$

where T is a delay between signal photons traversing the upper arm of the interferometer and signal photons traveling through the lower arm.

At the sample, the operator transformation is [24,25]

$$a_i(\Omega) \Rightarrow \tau a_i(\Omega) + f(\Omega), \quad (A9)$$

where τ is the reflectivity of the sample and the commutation relationship fulfills $[f(\Omega), f^\dagger(\Omega)] = \delta(\omega - \omega')$. Taking this into account, the operators a_{s_1}, just before the corresponding

input port of the polarization beam splitter (see the simple sketch in Fig. 9), read

$$
\begin{aligned}
(i)\, &b_s(\Omega) \\
&\Rightarrow (ii)\, [U(\Omega)b_s(\Omega) + V(\Omega)b_i^\dagger(-\Omega)]\exp[ik_s(\Omega)L] \\
&\Rightarrow (iii)\, a_{s_1}(\Omega) = [U(\Omega)b_s(\Omega) + V(\Omega)b_i^\dagger(-\Omega)]\exp\left[ik_s(\Omega)L + ik_s^0(\Omega)z_1\right].
\end{aligned}
\tag{A10}
$$

The three expressions correspond to the operators (i) at the input face of the nonlinear crystal, (ii) at the output face, and (iii) before the polarizing beam splitter.

The operators a_{s_2}, just before the corresponding input port of the polarization beam splitter, read

$$
\begin{aligned}
(i)\, &b_i(\Omega) \\
&\Rightarrow (ii)\, [U(\Omega)b_i(\Omega) + V(\Omega)b_s^\dagger(-\Omega)]\exp[ik_i(-\Omega)L] \\
&\Rightarrow (iii)\, [U(\Omega)b_i(\Omega) + V(\Omega)b_s^\dagger(-\Omega)]\exp\left[ik_i(-\Omega)L + ik_i^0(-\Omega)z_2\right] \\
&\Rightarrow (iv)\, \tau[U(\Omega)b_i(\Omega) + V(\Omega)b_s^\dagger(-\Omega)]\exp\left[ik_i(-\Omega)L + ik_i^0 i(-\Omega)z_2\right] + f(-\Omega) \\
&\Rightarrow (v)\, \tau[U(\Omega)b_i(\Omega) + V(\Omega)b_s^\dagger(-\Omega)]\exp\left[ik_i(-\Omega)L + ik_i^0(-\Omega)(z_2 + z_3)\right] + f(-\Omega)\exp\left[ik_i^0(-\Omega)z_3\right] \\
&\Rightarrow (vi)\, U(\Omega)c_s(\Omega)\exp[ik_s(\Omega)L] + V(\Omega)\tau^*[U^*(-\Omega)b_i^\dagger(-\Omega) + V^*(-\Omega)b_s(\Omega)] \\
&\qquad \times \exp\left[ik_s(\Omega)L - ik_i(\Omega)L - ik_i^0(\Omega)(z_2 + z_3)\right] + V(\Omega)f^\dagger(\Omega)\exp\left[ik_s(\Omega)L - ik_i^0(\Omega)z_3\right] \\
&\Rightarrow (vii)\, a_{s_2} = U(\Omega)c_s(\Omega)\exp\left[ik_s(\Omega)L + ik_s^0(\Omega)z_4\right] + V(\Omega)\tau^*[U^*(-\Omega)b_i^\dagger(-\Omega) + V^*(-\Omega)b_s(\Omega)] \\
&\qquad \times \exp[ik_s(\Omega)L - ik_i(\Omega)L - ik_i^0(\Omega)(z_2 + z_3) + ik_s^0(\Omega)z_4] + V(\Omega)f^\dagger(\Omega)\exp\left[ik_s(\Omega)L - ik_i^0(\Omega)z_3 + ik_s^0(\Omega)z_4\right]
\end{aligned}
\tag{A11}
$$

The six expressions correspond to the operators (i) at the input face of the first nonlinear crystal, (ii) at the output face, (iii) before the sample, (iv) after the sample, (v) before the second nonlinear crystal, (vi) after the nonlinear crystal, and (vii) before the PBS.

The flux of photons of both signal beams are

$$
N_{s_1}(t) = \langle a_{s_1}^\dagger(t)a_{s_1}(t)\rangle = \frac{1}{2\pi}\int d\Omega |V(\Omega)|^2 = \frac{(\sigma L)^2}{2\pi}\int d\Omega\, \mathrm{sinc}^2\left(\frac{DL\Omega}{2}\right) = \frac{\sigma^2 L}{D}
\tag{A12}
$$

and

$$
N_{s_2}(t) = \langle a_{s_2}^\dagger(t)a_{s_2}(t)\rangle = \frac{1}{2\pi}\int d\Omega |V(\Omega)|^2[1 + |\tau|^2|V(\Omega)|^2] \sim \frac{1}{2\pi}\int d\Omega |V(\Omega)|^2 = \frac{\sigma^2 L}{D}.
\tag{A13}
$$

Under our experimental conditions, the flux of signal photons is the same in both arms of the interferometer [see Fig. 2(c)]. The correlation function $|\langle a_{s_1}^\dagger(t)a_{s_2}(t)\rangle|$ writes

$$
\begin{aligned}
|\langle a_{s_1}^\dagger(t+T)a_{s_2}(t)\rangle| &= \frac{|\tau|}{2\pi}\left|\int d\Omega |V(\Omega)|^2 \exp\left[i(\omega_s + \Omega)T - ik_i(\Omega)L - ik_i^0(\Omega)(z_2 + z_3) + ik_s^0(\Omega)z_4\right]\right| \\
&= \frac{|\tau|}{2\pi}\int d\Omega\, \mathrm{sinc}^2\left(\frac{DL\Omega}{2}\right)\exp\left[i\frac{\Omega}{c}(z_1 + cT) - (z_4 - cN_i L - z_2 - z_3)\right].
\end{aligned}
\tag{A14}
$$

Therefore, we obtain

$$
\left|g_{s_1,s_2}^{(1)}(T)\right| = \frac{\left|\langle a_{s_1}^\dagger(t+T)a_{s_2}(t)\rangle\right|}{\sqrt{\langle a_{s_1}^\dagger(t)a_{s_1}(t)\rangle}\sqrt{\langle a_{s_2}^\dagger(t)a_{s_2}(t)\rangle}} = \mathrm{tri}\left\{\frac{1}{cDL}[(z_1 + cT) - (z_4 - cN_i L - z_2 - z_3)]\right\},
\tag{A15}
$$

where "tri" is the triangular function. This expression describes the result shown in Fig. 5, where one can see the triangular shape of the correlation function. The temporal resolution of the OCT scheme is given by DL, which is the inverse bandwidth of the source of photons. The spatial resolution in free space is thus cDL.

---

[1] D. Huang, E. A. Swanson, C. P. Lin, J. S. Schuman, W. G. Stinson, W. Chang, M. R. Hee, T. Flotte, K. Gregory, C. A. Puliafito, and J. G. Fujimoto, Optical coherence tomography, Science **254**, 1178 (1991).

[2] X. Y. Zou, L. J. Wang, and L. Mandel, Induced Coherence and Indistinguishability in Optical Interference, Phys. Rev. Lett. **67**, 318 (1991).

[3] L. Mandel and E. Wolf, *Optical Coherence and Quantum Optics* (Cambridge University Press, Cambridge, 1995).

[4] Here we follow Glauber's notation [5]. The order of the coherence or correlation function corresponds to the number of fields E^-, or fields E^+, present in the definition of the coherence function. Therefore, $\langle E^- E^+ \rangle$ is designated as first-order coherence, while $\langle E^- E^- E^+ E^+ \rangle$ corresponds to second-order coherence. For other authors, such as Mandel and Wolf [3], coherence order corresponds to the number of fields E^- and E^+ present in the definition of the coherence function. Therefore, they designate $\langle E^- E^+ \rangle$ as second-order coherence and $\langle E^- E^- E^+ E^+ \rangle$ as fourth-order coherence.

[5] R. J. Glauber, The quantum theory of optical coherence, Phys. Rev. **130**, 2529 (1963); Coherent and incoherent states of the radiation field, **131**, 2766 (1963).

[6] Z. Y. Ou, L. J. Wang, X. Y. Zou, and L. Mandel, Coherence in two-photon down-conversion induced by a laser, Phys. Rev. A **41**, 1597 (1990).

[7] X. Y. Zou, T. P. Grayson, and L. Mandel, Observation of Quantum Interference Effects in the Frequency Domain, Phys. Rev. Lett. **69**, 3041 (1992).

[8] A. V. Belinsky and D. N. Klyshko, Interference of classical and non-classical light, Phys. Lett. A **166**, 303 (1992).

[9] H. M. Wiseman and K. Mølmer, Induced coherence with and without induced emission, Phys. Lett. A **270**, 245 (2000).

[10] M. V. Chekhova and Z. Y. Ou, Nonlinear interferometers in quantum optics, Adv. Opt. Photon. **8**, 104 (2016).

[11] A. Heuer, R. Menzel, and P. W. Milonni, Induced Coherence, Vacuum Fields, and Complementarity in Biphoton Generation, Phys. Rev. Lett. **114**, 053601 (2015).

[12] A. Heuer, R. Menzel, and P. W. Milonni, Complementarity in biphoton generation with stimulated or induced coherence, Phys. Rev. A **92**, 033834 (2015).

[13] D. A. Kalashnikov, A. V. Paterova, S. P. Kulik, and L. A. Krivitsky, Infrared spectroscopy with visible light, Nat. Photon. **10**, 98 (2016).

[14] G. Barreto-Lemos, V. Borish, G. D. Cole, S. Ramelow, R. Lapkiewicz, and A. Zeilinger, Quantum imaging with undetected photons, Nature (London) **512**, 409 (2014).

[15] A. Hochrainer, M. Lahiri, R. Lapkiewicz, G. Barreto-Lemos, and A. Zeilinger, Interference fringes controlled by noninterfering photons, Optica **4**, 341 (2017).

[16] M. B. Nasr, B. E. A. Saleh, A. V. Sergienko, and M. C. Teich, Demonstration of Dispersion-Canceled Quantum-Optical Coherence Tomography, Phys. Rev. Lett. **91**, 083601 (2003).

[17] A. F. Abouraddy, M. B. Nasr, B. E. A. Saleh, A. V. Sergienko, and M. C. Teich, Quantum-optical coherence tomography with dispersion cancellation, Phys. Rev. A **65**, 053817 (2002).

[18] Y. Wang, J. S. Nelson, Z. Chen, B. Jin Reiser, R. S. Chuck, and R. S. Windeler, Optimal wavelength for ultrahigh-resolution optical coherence tomography, Opt. Express **11**, 1411 (2003).

[19] B. I. Erkmen and J. H. Shapiro, Phase-conjugate optical coherence tomography, Phys. Rev. A **74**, 041601(R) (2006).

[20] J. Le Gouët, D. Venkatraman, F. N. C. Wong, and J. H. Shapiro, Experimental realization of phase-conjugate optical coherence tomography, Opt. Lett. **35**, 1001 (2010).

[21] P. Navez, E. Brambilla, A. Gatti, and L. A. Lugiato, Spatial entanglement of twin quantum images, Phys. Rev. A **65**, 013813 (2001).

[22] E. Brambilla, A. Gatti, M. Bache, and L. A. Lugiato, Simultaneous near-field and far-field spatial quantum correlations in the high-gain regime of parametric down-conversion, Phys. Rev. A **69**, 023802 (2004).

[23] J. P. Torres, K. Banaszek, and I. A. Walmsley, Engineering nonlinear optic sources of photonic entanglement, Prog. Optics **56**, 227 (2011).

[24] H. A. Haus, *Electromagnetic Noise and Quantum Optical Measurements* (Springer-Verlag, Berlin, 2000).

[25] R. W. Boyd, G. S. Agarwal, K. W. C. Chan, A. K. Jha, and M. N. Sullivan, Propagation of quantum states of light through absorbing and amplifying media, Opt. Commun. **281**, 3732 (2008).

[26] A. Heuer, S. Raabe, and R. Menzel, Phase memory across two single-photon interferometers including wavelength conversion, Phys. Rev. A **90**, 045803 (2014).

[27] X. Y. Zou, T. Grayson, G. A. Barbosa, and L. Mandel, Control of visibility in the interference of signal photons by delays imposed on the idler photons, Phys. Rev. A **47**, 2293 (1993).

[28] S. Fuchs, M. Wünsche, J. Nathanael, J. J. Abel, C. Rödel, J. Biedermann, J. Reinhard, U. Hübner, and G. G. Paulus, Optical coherence tomography with nanoscale axial resolution using a laser-driven high-harmonic source, Optica **4**, 903 (2017).

[29] S. Fuchs, C. Rödel, A. Blinne, U. Zastrau, M. Wünsche, V. Hilbert, L. Glaser, J. Viefhaus, E. Frumker, P. Corkum, E. Förster, and G. G. Paulus, Nanometer resolution optical coherence tomography using broad bandwidth XUV and soft x-ray radiation, Sci. Rep. **6**, 20658 (2016).

[30] M. Hendrych, X. Shi, A. Valencia, and J. P. Torres, Broadening the bandwidth of entangled photons: A step towards the generation of extremely short biphotons, Phys. Rev. A **79**, 023817 (2009).

[31] P. Abolghasem, M. Hendrych, X. Shi, J. P. Torres, and A. S. Helmy, Bandwidth control of paired photons generated in monolithic Bragg reflection waveguides, Opt. Lett. **34**, 2000 (2009).

[32] J. H. Shapiro, D. Venkatraman, and F. N. C. Wong, Classical imaging with undetected photons, Sci. Rep. **5**, 10329 (2015).